

Article

Reactive Fe-O-Ce Sites in Ceria Catalysts for Soot Oxidation

Boyun Li ¹, Abhishek Raj ², Eric Croiset ¹ and John Z. Wen ^{2,*}

¹ Department of Chemical Engineering, University of Waterloo, 200 University Avenue West, Waterloo, ON N2L3G1, Canada; b264li@uwaterloo.ca (B.L.); ecroiset@uwaterloo.ca (E.C.)

² Department of Mechanical & Mechatronics Engineering, University of Waterloo, 200 University Avenue West, Waterloo, ON N2L3G1, Canada; rajabhi08@gmail.com

* Correspondence: john.wen@uwaterloo.ca; Tel.: +1-519-8884567 (ext. 32295)

Received: 31 August 2019; Accepted: 25 September 2019; Published: 28 September 2019



Abstract: This study investigates the role of oxygen vacancy on Fe-doped CeO₂ catalyst activity for soot oxidation. The oxygen vacancy was assessed through Ce³⁺ content. The Fe content was varied between 0 and 30% for two catalyst preparation methods, co-precipitation (CP) and solution combustion synthesis (SCS). X-ray photoelectron spectroscopy indicates that ceria exists as both Ce⁴⁺ and Ce³⁺, while iron is present only as Fe³⁺. The catalyst's activity was evaluated by ignition (T10) and combustion (T50) temperatures using thermogravimetric analysis. Optimum Fe contents yielding the highest activity were found to be 10% and 5% for CP and SCS catalysts, respectively. The surface area and morphology showed a moderate effect on catalyst activity, because catalytic soot oxidation involves solid–solid contact. More importantly, regardless of the fabrication method, it was found that Ce³⁺ content, which is closely related to oxygen vacancies, plays the most important role in affecting the catalyst activity.

Keywords: soot oxidation; catalytic; heterogeneous catalysis; oxygen vacancies; iron-doped ceria catalyst; ceria

1. Introduction

Particulate matters or PM (consisting primarily of soot) can cause serious environmental and health problems, such as lung cancer [1–3]. Particulate matters or PM emission can be controlled by processing the exhaust gas through a diesel particulate filters (DPF). DPF with a monolithic geometry have been used to capture and oxidize fine carbon particles [4]. The desired temperature of soot combustion is above 600 °C, but the temperature of exhaust gas is around 200–500 °C [5–7]. It is necessary to introduce catalysts to effectively decrease the soot oxidation temperature and improve the reactor efficiency. Usually, the catalyst is coated on the monolith wall of the DPF [4–11]. After a period of soot deposition, a pressure drop may occur through the DPF, making it necessary to regenerate the DPF periodically [11].

The desired catalysts for soot oxidation should have high activity and suitable stability but low cost, which makes ceria-based catalyst particularly attractive [12–15]. Ceria-based catalysts have been applied on DPF to study their catalytic activity for soot oxidation [16–19]. Ceria has been found to act as an active oxygen producer to promote the formation of reactive oxygen species and transfer them to soot-catalyst interface to oxidize soot, which is described in the active oxygen-assisted oxidation mechanism [12,15]. The oxygen species can be transferred between the oxidized state Ce⁴⁺ and reduced state Ce³⁺ [1,2,20–22], thus forming oxygen vacancies through Ce⁴⁺ to Ce³⁺ reduction, and adsorbing gaseous oxygen via Ce³⁺ to Ce⁴⁺.

The activity of ceria-based catalysts can be further improved through doping other metal additives into the ceria lattice, in order to enhance the oxygen storage capability (OSC) and oxygen mobility [15,22]. Transition metal doping has been reported to produce more active sites over the catalyst surface and

promote catalytic soot oxidation [20,23–25]. Iron, in particular, is prominent because it can improve the catalyst activity due to its good redox ability—the oxygen species can alternate between Fe^{3+} and Fe^{2+} [2,15,26]. The mechanism of iron-doped ceria catalysts has been investigated by Zhang et al. [20], indicating that the redox cycle of iron played an important role in this reaction. Fe^{3+} can provide its bonded active oxygen to oxidize soot, along with its reduction to Fe^{2+} . Fe^{2+} can then be re-oxidized to Fe^{3+} with the interaction of Ce [15,20]. The number of active Fe-O-Ce sites can vary due to different ratios of iron doping, as iron doping can distort the fluorite lattice and create oxygen vacancies to varying degrees. Thus, the ratio of iron doping in ceria affects the catalyst activity and need be optimized with reaction conditions.

As the catalytic soot oxidation is a surface sensitive reaction, the contact points between soot and catalyst particles have a great impact on activity [1]. Nano-sized materials result in a high surface-to-volume ratio and make their chemical and physical properties more size and shape dependent [27–29]. More specifically, the quantum size effects and higher surface areas make these nanostructured catalysts possess more potential contact points between soot and catalyst particles while their meso-scale pores (with diameters between 2 and 50 nm) can promote the oxygen diffusion through catalysts [27]. To enhance the interactions between soot and catalyst, different morphologies of ceria-based catalysts have been fabricated by several preparation methods [30–36]. It is found that different morphologies exhibit distinct catalytic activity, which is strongly dependent on their physical and chemical surface properties [15]. Among these preparation methods, the co-precipitation (CP) method has been widely used for catalyst preparation due to the formation of higher surface area and smaller crystal size [20]. Alternatively, solution combustion synthesis (SCS) is a time effective and energy saving method to produce nano-sized porous catalysts [37]. Herein, these two preparation methods have been chosen in this study to investigate the morphologies influence on catalyst activity.

Different iron doping ratios and morphologies would change the surface properties and oxygen vacancies of catalysts, which has influence on catalyst activity [38]. Kattal et al. found that increasing oxygen vacancies induces more active oxygen for $\text{CeO}_2\text{-La}_2\text{O}_3$ catalyst for soot oxidation [39]. $\text{MnO}_x\text{-CeO}_2$ mixed oxides were also investigated for soot oxidation, while it was suggested that an improved mobility and transformation of oxygen vacancies both promote the catalyst activity [40]. Another study using Ag-CeO₂ catalysts showed that an appropriate Ag incorporation (5% wt.%) in CeO₂ is crucial in creating surface oxygen vacancies and helps O_2^- generation [41]. By contrast, an investigation of $\text{ZrO}_x\text{-CeO}_2$ catalyst revealed that formation of excessive surface oxygen vacancies hardly benefits the soot oxidation under low concentrations of O₂ (1% O₂/N₂ at 500 mL/min), because of the production of low active O²⁻ sites [42]. The above-mentioned studies showed a relation between oxygen vacancy and catalyst activity. However, the effect of oxygen vacancy on soot oxidation by altering the catalyst morphologies along with different Fe doping ratios is still poorly understood. Therefore, this study aims at investigating the role of oxygen vacancy on catalyst activity through varying the Fe doping ratio and tailoring the catalyst morphology.

2. Results and Discussion

2.1. Characterization

The crystal structure of all catalysts was studied by X-ray powder diffraction (XRD). The XRD patterns of iron-doped cerium oxide catalysts prepared by SCS and CP methods are depicted in Figure 1. The main diffraction peaks could be attributed to (111) (200) (220) (311) (222) (400) (331) (420) planes, referring to a typical face-centered cubic fluorite structure matching the spectra for pure cerium oxide (JCPDS NO. 34-0394) [43]. The characteristic peaks shifted to higher 2θ diffraction angle with iron doping, and no peaks of Fe_2O_3 were observed, suggesting the uniform incorporation of iron into cerium oxide lattice and the formation of solid solution, thus the catalyst could be represented by $\text{Fe}_x\text{Ce}_{100-x}$ [2,26,39,44,45]. Arguably, Aneggi et al. [46] reported that it was possible that only a small amount of Fe dissolves into the ceria lattice. Barbato et al. [47] found that Fe_2O_3 could be encapsulated by ceria, making it undetectable by XRD. Further investigation on the exact formulation of the iron-doped

ceria catalyst is needed. The absence of characteristic peaks of iron oxide could also result from the absence of iron oxide on the surface or from the crystal being too small to be detected by XRD.

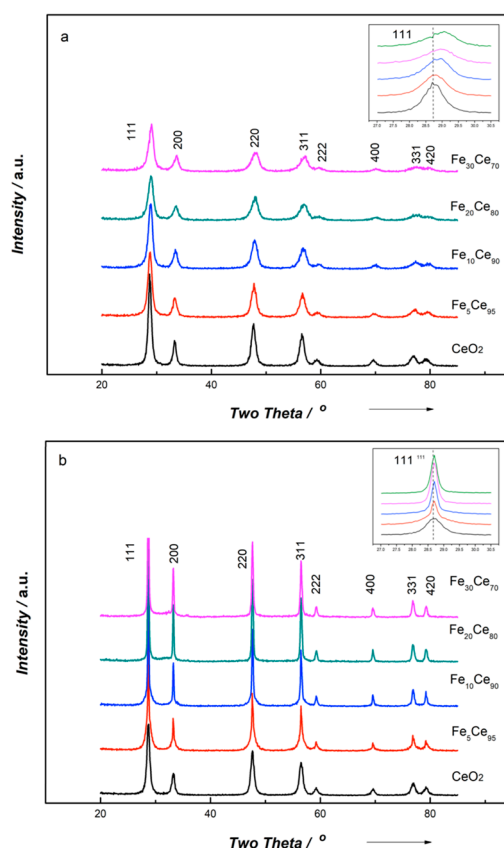


Figure 1. Powder X-ray diffraction patterns of (a) the co-precipitation method and (b) the solution combustion synthesis method.

The textural properties of the catalysts are listed in Table 1; the crystal size was calculated using the Scherrer equation, while the unit lattice parameter was calculated by Bragg's law using the strongest peak (111). From Table 1, it is clear that CP catalysts lead to smaller crystal size than for SCS catalysts. In addition, compared to pure ceria, iron doping results in smaller crystal size for CP catalyst, but a much higher crystal size for SCS catalyst. Table 1 also shows that the lattice parameter slightly decreases with more iron doping. This is because of the smaller iron atoms (Fe^{3+} -0.64 Å, Fe^{2+} -0.74 Å) substituting larger ceria sites (0.97 Å) in the lattice to form Ce-Fe-O solid solution [26]. These results also indicated the incorporation of iron into ceria lattice.

Table 1. Textural properties of as-derived catalysts.

| Catalyst | Crystal Size [nm] | Lattice Parameter [Å] | S_{BET} [m^2g^{-1}] | Pore Size [nm] |
|--|-------------------|-----------------------|--|----------------|
| CeO ₂ -CP | 11.71 | 5.38 | 73 | 2.46 |
| Fe ₅ Ce ₉₅ -CP | 9.11 | 5.36 | 87 | 3.48 |
| Fe ₁₀ Ce ₉₀ -CP | 8.63 | 5.34 | 94 | 3.49 |
| Fe ₂₀ Ce ₈₀ -CP | 7.96 | 5.33 | 87 | 5.60 |
| Fe ₃₀ Ce ₇₀ -CP | 7.89 | 5.32 | 65 | 3.51 |
| CeO ₂ -SCS | 13.33 | 5.39 | 38 | 3.63 |
| Fe ₅ Ce ₉₅ -SCS | 30.59 | 5.38 | 39 | 4.61 |
| Fe ₁₀ Ce ₉₀ -SCS | 31.53 | 5.37 | 20 | 3.66 |
| Fe ₂₀ Ce ₈₀ -SCS | 32.79 | 5.37 | 3 | 4.56 |
| Fe ₃₀ Ce ₇₀ -SCS | 34.15 | 5.37 | 2 | 3.82 |

As shown in Table 1, catalysts made using the CP method reveal a higher surface area than those made by the SCS method. $\text{Fe}_{10}\text{Ce}_{90}$ -CP and $\text{Fe}_5\text{Ce}_{95}$ -SCS yielded the highest specific surface area within their preparation method, and $\text{Fe}_{10}\text{Ce}_{90}$ -CP showed the largest surface area ($94 \text{ m}^2\text{g}^{-1}$) among them all. Accordingly, the introduction of iron enlarged the surface area of the CP catalyst. For SCS catalysts, only 5% iron doping showed slight increase of surface area compared to pure CeO_2 , but other ratios of doping led to a surface area decrease. It was also noticed that the surface area greatly dropped with greater than 20% iron doping, especially for the SCS method. The pore diameters of both CP and SCS catalysts are around 3–5 nm.

Scanning electron microscopy (SEM) was performed to explore the surface morphologies of catalysts. In Figure 2, both pictures clearly show the nanoparticle morphologies: the CP method produced uniform spherical morphology with some agglomeration, while the catalyst made by the SCS method reported a spongy structure. The spherical morphology for the CP method was a result of the precipitants' nucleation, and these small particles yielded a higher surface area. The foamy and highly porous spongy structure is a more unpredictable structure than that made from the SCS method, which was due to the combustion procedure, in which the reacting precursor releases lots of gaseous products in a short time. Moreover, these bigger openings got from this morphology can be large enough (around 250 nm diameter) for soot particles (typical size around 25 nm) to penetrate, thus creating more contact points between soot and catalyst particles.

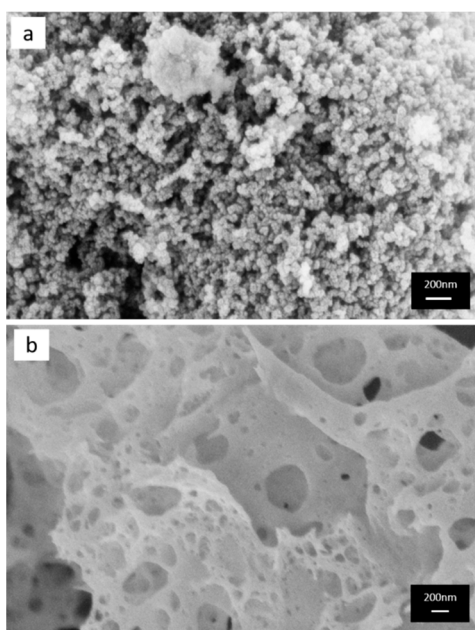


Figure 2. FE-SEM images of (a) the co-precipitation method and (b) the solution combustion synthesis method.

X-ray photoelectron spectroscopy (XPS) analysis was undertaken to study the surface properties of catalysts in terms of their oxidation state and surface oxygen vacancies. Figure 3 shows the Ce 3d spectra of all catalysts. The Ce 3d spectra could be curve-fitted into eight peaks corresponding to the spin-orbit splitting of Ce $3d_{5/2}$ and Ce $3d_{3/2}$, which were labelled as “u” and “v”, respectively [48]. The peaks labelled as v0, v2, v3, u0, u2, u3, with binding energy (BE) around 882, 888, 898, 900, 907, 916 eV, correspond to the Ce^{4+} species, and peaks labelled as v1, u1, with binding energy of 884 and 902 eV, are ascribed to Ce^{3+} species. The analysis of XPS spectra suggested that Ceria existed as both Ce^{3+} and Ce^{4+} , but primarily in Ce^{4+} state. When Ce^{4+} transferred to Ce^{3+} , oxygen vacancies associated with Ce^{3+} could be generated to potentially adsorb oxygen and provide it for soot oxidation. Therefore, the existence of Ce^{3+} becomes important to indicate the generation of oxygen vacancies [2,26]. The calculations of integrated peak areas were used to get a quantitative analysis of a selected element. In this way, the ratio of Ce^{3+} area to total area including Ce^{3+} and Ce^{4+} was applied to estimate the

ratio of Ce^{3+} ; the results are given in Table 2. From Table 2, all Ce^{3+} percentages are around 20%, CP catalysts are between 19–25%, and SCS catalysts are between 17–27%. Ce^{3+} content has a similar trend for both CP and SCS catalysts, which is that Ce^{3+} goes up to a maximum value and then goes down. The maximum Ce^{3+} value for CP catalysts is 24.9% with 10% iron doping, and is 27.1% with 5% iron doping for SCS catalysts. Among all catalysts, $\text{Fe}_5\text{Ce}_{95}$ -SCS gives the highest Ce^{3+} percentage, higher than $\text{Fe}_{10}\text{Ce}_{90}$ -CP. Therefore, it can be deduced that $\text{Fe}_5\text{Ce}_{95}$ -SCS has the highest concentration of oxygen vacancies.

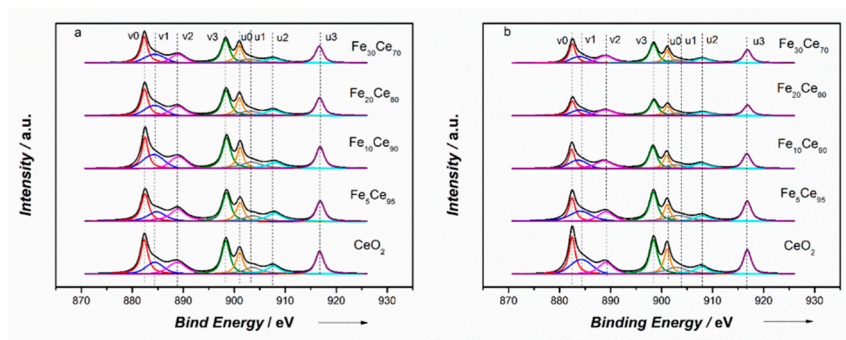


Figure 3. XPS spectra of Ce3d: (a) Co-precipitation method, (b) solution combustion synthesis method.

Table 2. Curve fitting results of Ce3d and O1s on obtained catalysts.

| Catalyst | Preparation Method | Ce^{3+} Content [%] | O_α Content [%] | I_{596}/I_{463} |
|-----------------------------------|--------------------|------------------------------|-------------------------------|-------------------|
| CeO ₂ | CP | 20.1 | 31.5 | 0.023 |
| | SCS | 24.5 | 33.3 | 0.028 |
| Fe ₅ Ce ₉₅ | CP | 19.7 | 32.8 | 0.037 |
| | SCS | 27.1 | 39.0 | 0.032 |
| Fe ₁₀ Ce ₉₀ | CP | 24.9 | 37.5 | 0.029 |
| | SCS | 20.4 | 33.8 | 0.029 |
| Fe ₂₀ Ce ₈₀ | CP | 21.4 | 35.5 | 0.038 |
| | SCS | 17.1 | 29.1 | 0.021 |
| Fe ₃₀ Ce ₇₀ | CP | 20.5 | 33.3 | 0.013 |
| | SCS | 16.9 | 28.1 | 0.011 |

The Fe 2p spectra in Figure 4 show the characteristic Fe 2p_{3/2} and Fe 2p_{3/1} peaks at binding energy of 711 and 724 eV, respectively. Two satellites peaks at 718 and 733 eV can be slightly distinguished. These peaks indicate the existence of Fe³⁺. The binding energy of Fe 2p decreased with more iron doping, further confirming that the Fe³⁺ was incorporated into CeO₂ lattice and formed a solid solution, as shown by the XRD results.

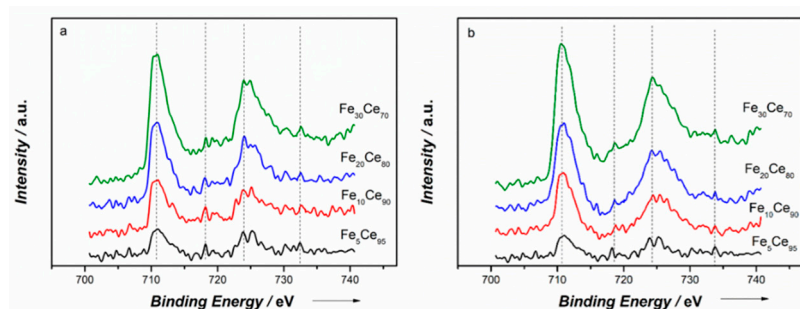


Figure 4. XPS spectra of Fe2p: (a) Co-precipitation method, (b) solution combustion synthesis method.

The O1s spectra showed two distinct peaks in Figure 5. The peak at higher binding energy (531.7 eV) referred to the surface oxygen species O_α , and the peak at lower binding energy (529.5 eV) is attributed

to the lattice oxygen O_{β} [33]. As Fe is added into CeO_2 , the main peak O_{β} shifted to higher binding energy, suggesting the chemical environment of lattice oxygen changed due to the incorporation of Fe [49]. The surface oxygen species O_{α} are critical for soot oxidation because they can become active and react with soot particles. The ratio of surface oxygen concentration to lattice oxygen concentration can be estimated by the integrated peak areas of O_{α} and O_{β} , and the results are shown in Table 2. For the CP method, O_{α} percentage- $O_{\alpha}/(O_{\alpha} + O_{\beta})$ increased to a maximum point (37.5%) at 10% iron doping, and then decreased. SCS catalysts showed similar behavior, where it reached a maximum value (39.0%) at 5% iron doping. $\text{Fe}_5\text{Ce}_{95}$ -SCS led to the highest surface oxygen concentration. These results agree well with concentration percentage of Ce^{3+} .

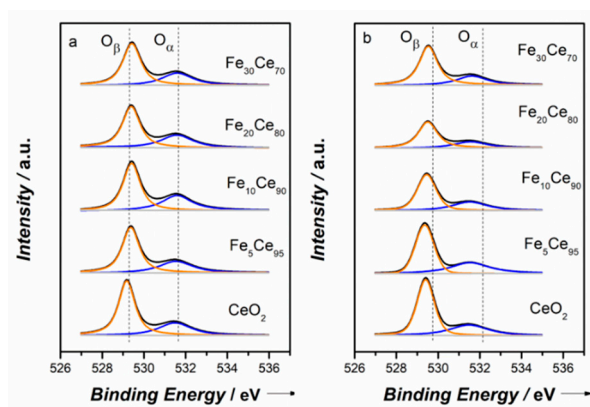


Figure 5. XPS spectra of O1s: (a) Co-precipitation method, (b) solution combustion synthesis method.

Raman spectroscopy was conducted to study the oxygen vacancies and active sites within the catalysts. Figure 6 shows the Raman spectra of $\text{Fe}_x\text{Ce}_{100-x}$ catalysts made by CP and SCS methods. The prominent band at $\sim 463\text{cm}^{-1}$ could be assigned to the first-order scattering F2g symmetric oxygen active mode around Ce^{4+} with a CeO_2 fluorite structure [50], which is in agreement with the XRD and XPS results. All catalysts' spectra are identical to that of pure CeO_2 , further indicating that iron has been incorporated into the CeO_2 lattice. Compared to the Raman spectra of pure CeO_2 , the F2g band shifted to lower frequency and broadened with an increase in iron doping, suggesting the lattice distortion is due to the incorporation of iron into CeO_2 fluorite lattice [35]. The intensity (I) of the Raman spectra decreased with increasing iron doping, indicating the structure change due to Fe incorporation and lower ceria content [26]. No peaks of Fe_2O_3 were observed, which is possibly due to the much weaker bands of Fe_2O_3 than CeO_2 and the formation of solid solution. Two weak bands at 261 and 596cm^{-1} were characteristic bands of second order scattering, which can represent the oxygen vacancies in the lattice [20]. The low intensity of oxygen vacancies showed in Raman spectra was because the sample was not outgassed, the intensity would be higher if the sample was outgassed at high temperature [44].

The 596cm^{-1} band exhibits the oxygen vacancies caused by Ce^{3+} ; thus, the value of I_{596}/I_{463} (as shown in Table 2) becomes important to evaluate the oxygen vacancies or amount of defects in the catalysts. Catalysts made by the two methods (CP and SCS) showed similar trend of I_{596}/I_{463} with increasing iron content; that is, increase first until a maximum is reached, and then drop down. This is because Fe prefers to occupy Ce sites in CeO_2 , and thus the oxygen vacancy concentration increases with more Fe doping. However, when the amount of Fe exceeded a critical value, Fe becomes interstitial in CeO_2 lattice, thus decreasing oxygen vacancy concentration [51]. The results showed that $\text{Fe}_{10}\text{Ce}_{90}$ -CP and $\text{Fe}_5\text{Ce}_{95}$ -SCS reached optimum I_{596}/I_{463} value within their preparation method. $\text{Fe}_5\text{Ce}_{95}$ -SCS obtained the maximum I_{596}/I_{463} value, indicating the highest oxygen vacancies.

Temperature-programmed reduction with hydrogen (H_2 -TPR) was applied to investigate the catalysts' reducibility. Figure 7 shows the overall TPR results for catalysts with different iron contents prepared by CP and SCS methods. Figures S1 and S2 in Supplementary Data show the deconvoluted TPR results for CP and SCS catalysts. Four peaks were identified in Figure 7, and represent the

reductions of (1) surface oxygen of ceria, (2) Fe_2O_3 to Fe_3O_4 , (3) Fe_3O_4 to FeO , and (4) bulk oxygen of ceria. The Supplementary Data also includes the amount of H_2 which was used for each of the four reduction processes.

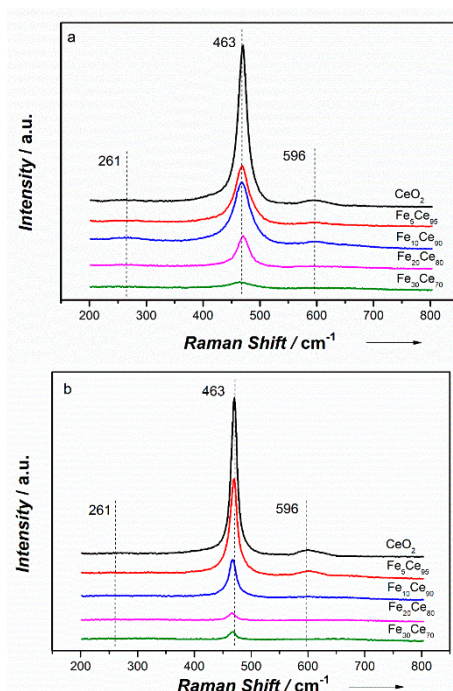


Figure 6. Raman spectra of (a) the co-precipitation method (b) the solution combustion synthesis method.

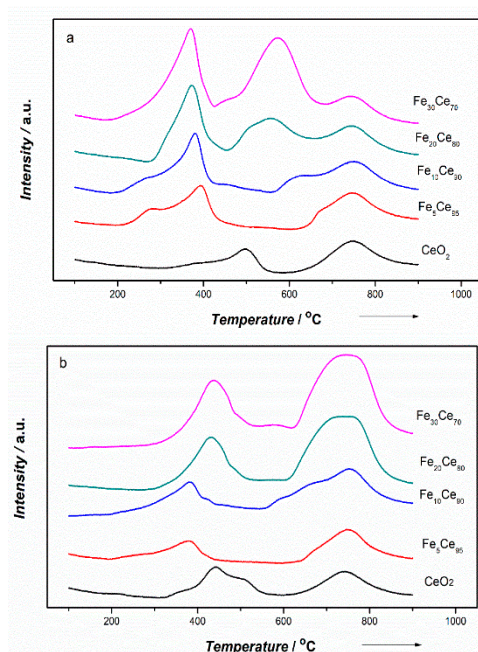


Figure 7. H_2 -TPR results of (a) the co-precipitation method and (b) the solution combustion synthesis method.

The trends corresponding to the reduction of surface oxygen of ceria (for these peaks at the lowest temperature) are similar for CP and SCS catalysts. Addition of 5% iron in ceria significantly shifts the reduction peak to a lower temperature: from 450–480 °C for pure ceria to 300–320 °C for Fe-ceria catalysts. However, Fe content beyond 5% has little effect on peak shifting for either catalyst. These peaks, corresponding to the reduction of bulk oxygen in ceria, do not show a clear temperature

shift when the Fe content is increased in both CP and SCS catalysts, remaining at about 750 °C. The comparison between these effects of Fe doping on shifting the reduction temperatures of two different catalysts likely indicates, adding iron in ceria (of both CP and SCS catalysts) changes the activity of surface oxygen, rather than that of the bulk oxygen, more significantly.

The reduction of Fe_2O_3 to Fe_3O_4 shows no peak shifting (located at 375 °C) when the Fe content increases to 10% for either the SCS or CP catalysts. For Fe content beyond 20%, the peak shifts to a higher temperature (~450 °C) for the SCS catalyst, whereas it remains at about 375 °C for the CP catalyst. Finally, the most important difference between these two catalysts exists during the reduction of Fe_3O_4 to FeO. For the SCS catalyst, the peak for this reduction process remains at 670–700 °C, irrespective of the Fe content. However, a peak shift towards a lower temperature occurs with increasing the Fe content for the CP catalyst, i.e., ~670 °C (similar to SCS) for the 5% Fe, ~625 °C for the 10% Fe, and 550–575 °C for the 20 and 30% Fe, respectively. In summary, the effects of Fe doping on the reduction of iron oxides are more significant when the Fe content is greater than 20%. During the catalyst fabrication, at a low Fe content (<10%), Fe is most likely present in a solid solution of ceria, whereas at a high Fe content (>20%), Fe atoms can aggregate and lead to the formation of iron oxides.

In Tables S1 and S2 of the Supplementary Material, the total amount of H_2 consumption increases when the Fe content increases, from ~1 mmol/g for pure ceria to ~3 mmol/g for the 30% Fe. Notably, the increased H_2 consumption results from the increasing contributions of these two iron oxide reductions, which account for more than 70% of the total H_2 consumption for the Fe content beyond 20%. It is noteworthy that single-phase iron oxides were not observed by XRD. This may be attributed to the formation of a very limited amount of iron oxides in the catalyst. In addition, the XRD spectrometer used in this study is more efficient for detecting catalyst surface properties. Iron oxides distributed in the bulk ceria catalyst are hard to identify. Herein, for a higher ratio of iron doping, the CP catalysts could have a co-existence of solid solution and aggregated iron oxide phases. However, for the SCS catalysts, no reduction peaks of iron oxides were observed, which is likely due to the absence of iron oxide or a limited amount of iron oxide.

2.2. Activity Study

Thermogravimetric analysis (TGA) experiments were carried out to investigate the catalyst activity for soot oxidation. Tight contact conditions were used to study the influence of iron doping ratio and morphology on catalyst activity. The result of soot conversion as a function of temperature is shown in Figure 8. Tight contact condition was used to explore the intrinsic activity of the catalysts because soot and catalysts were ground together to produce more contact points [22]. The activity of the catalyst was evaluated by the ignition temperature (T10) and combustion temperature (T50). T10 and T50 for tight contact conditions are summarized in Table 3. For comparison, non-catalytic soot oxidation was also conducted at the same reaction conditions.

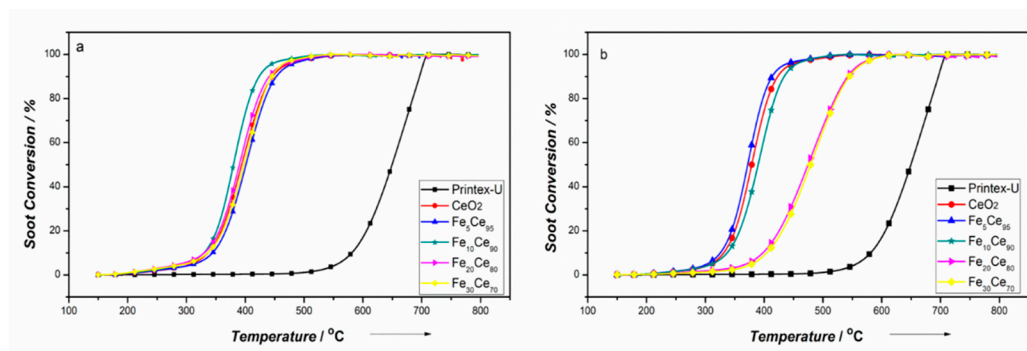


Figure 8. Soot conversion of tight contact condition: (a) Co-precipitation method, (b) solution combustion synthesis method.

Table 3. T10 and T50 for catalysts in tight contact condition.

| Tight | CeO ₂ | Fe ₅ Ce ₉₅ | Fe ₁₀ Ce ₉₀ | Fe ₂₀ Ce ₈₀ | Fe ₃₀ Ce ₇₀ | Printex-U |
|-------------|------------------|----------------------------------|-----------------------------------|-----------------------------------|-----------------------------------|-----------|
| T10-CP(°C) | 335.8 ± 1.2 | 342.4 ± 2.8 | 328.1 ± 1.9 | 329.3 ± 1.6 | 333.1 ± 3.5 | 581 ± 2.3 |
| T10-SCS(°C) | 328.7 ± 2.5 | 323.6 ± 1.7 | 336.0 ± 1.2 | 396.8 ± 2.4 | 400.9 ± 3.7 | 581 ± 2.3 |
| T50-CP(°C) | 393.1 ± 0.7 | 400.2 ± 1.3 | 377.5 ± 2.0 | 388.5 ± 1.1 | 396.4 ± 1.0 | 649 ± 3.1 |
| T50-SCS(°C) | 376.2 ± 2.0 | 371.5 ± 0.8 | 387.5 ± 1.8 | 472.8 ± 1.9 | 476.1 ± 2.3 | 649 ± 3.1 |

From Figure 8, it is obvious that soot oxidation temperatures decreased significantly when adding catalyst compared to non-catalytic soot oxidation. Different iron doping ratios and morphologies have distinct effects on catalyst activity. CP and SCS catalysts showed similar trend of T10 and T50 with different iron doping ratio, which decreased first to a threshold then began to increase. The minimum temperature in T10 and T50 for CP catalysts are T10~328 °C and T50~378 °C with 10% iron doping, and for SCS catalysts, they are T10~324 °C and T50~372 °C with 5% iron doping. It is noted that when doping ratio exceeded 20% for SCS catalysts, the catalyst activity greatly reduced (decreased by about 70 °C). Comparing CP to SCS catalysts, it is interesting to find that SCS catalyst performed better than CP catalyst with low Fe doping (<5%) despite their lower surface area. However, this situation changed when Fe content increased from 10% to 30%, CP catalysts became better performing than SCS catalysts of the same composition. This makes the surface area not the determining factor for catalytic soot oxidation. Although this reaction is surface sensitive, what matters most is the contact between solid soot and catalyst particles, making the available surface for contact points become important. As seen from Table 1, the pore size of CP and SCS catalysts are around 3–5 nm, which is too small for soot particles (around 25 nm) to go through. Although SCS catalysts had a spongy structure with lower surface area, many openings (~250 nm) resulted from the combustion process could easily let soot particles penetrate in to increase the contact points and possibly provide more adsorbed oxygen to the contact points and facilitate the oxygen diffusion through the catalyst [22]. However, when the iron content exceeds 20%, the Brunauer–Emmett–Teller (BET) surface area for SCS catalysts degrade significantly (only 2–3 m²g⁻¹). This makes the available contact points become very limited, resulting in a reduced activity performance.

XRD results showed that Fe was successfully incorporated into CeO₂ lattice for both CP and SCS catalysts. For CP catalysts, the crystal size decreased with introduction of iron, implying that iron incorporation could inhibit crystal growth. In this way, the smaller crystal size and higher surface area can benefit oxygen diffusion and increase contact points. On the contrary, XRD pattern showed that crystal size grew with more Fe doping for SCS catalysts. Crystal growth can be an obstacle for good catalytic performance. The spherical structure of CP catalysts (shown in SEM image), resulting from the nucleation of the precipitates, can explain their higher surface area.

XPS results indicate that 10%-CP and 5%-SCS iron doping had the highest Ce³⁺ and O_α ratios on the surface among their own preparation method, which meant that the oxygen vacancies were maximized at these ratios. The trend of Ce³⁺ and O_α ratio follows the trend of T10 and T50, and hence follows the catalyst activity. Raman results and I₅₉₆/I₄₆₃ values further confirmed oxygen vacancies, and Fe₁₀Ce₉₀-CP and Fe₅Ce₉₅-SCS showed the highest oxygen vacancies within their own preparation method. Figure 9 shows the relation between Ce³⁺ percentage and T10, T50. It is noticed that the activity (through T10 and T50) is really directly dependent on Ce³⁺, irrespective of the preparation method. The ratio of Ce³⁺ can represent the availability of oxygen vacancies [50], as it is reported that higher Ce³⁺ concentrations indicate more oxygen vacancies on the catalyst surface [15,36,38]. Therefore, oxygen vacancies on the surface is found to be the determining factor for catalyst activity. With more Ce³⁺ or oxygen vacancy concentration, both T10 and T50 decreased in a similar fashion. Figure 9 shows that there is a threshold of around 20% Ce³⁺, below which the catalyst activity rapidly deteriorates with further decreasing Ce³⁺ content, as indicated by the sharp drops in T10 and T50 at low Ce³⁺ content (T50: 476 to 393 °C). The samples with low Ce³⁺ also correspond to the lowest BET surface area (2–3 m²g⁻¹), which could also contribute to the lower activity. However, because the

catalytic soot oxidation involves contact between two solids, the BET surface area is less likely to play the most important role. Thus, the lower activities associated with Fe₂₀Ce₈₀-SCS and Fe₃₀Ce₇₀-SCS are attributed more to the low Ce³⁺ content than the low BET surface area. Above 20% Ce³⁺, T10 and T50 would still decrease with increasing Ce³⁺ content, but at a much-reduced rate (T50: 393 to 372 °C). This meant that Ce³⁺ content, and hence oxygen vacancy, has a great influence on catalyst activity. More oxygen vacancies facilitate adsorbing more oxygen species from gaseous oxygen, which then diffuse through the crystalline structure to the contact point between soot and catalyst and oxidize soot. Due to the presence of Ce³⁺ and Ce⁴⁺, the reaction proceeds through redox mechanism. According to the mechanism study by Zhang et al. [20] redox cycle between Fe²⁺ and Fe³⁺ also participates in this soot oxidation and formed Fe-O-Ce bond, suggesting a synergetic effect of Fe and Ce interaction. When Fe³⁺ provided one O to oxidize soot, Fe³⁺ became Fe²⁺. The Ce⁴⁺ on the neighboring site can supply one O to Fe²⁺, changing it to Fe³⁺ through the reduction of Ce⁴⁺ to Ce³⁺. Then adsorbing one O from bulk could oxidize Ce³⁺ to Ce⁴⁺ again. The oxygen species are transferred within the catalyst lattice to reach the interface between soot and catalyst. The as-derived catalysts have different crystal structures due to various ratios of iron doping, which can cause lattice distortion and surface defects, thus changing the bond between Ce and O and creating some oxygen vacancies on the catalyst surface. This is the reason certain ratios of iron doping can improve the catalyst activity.

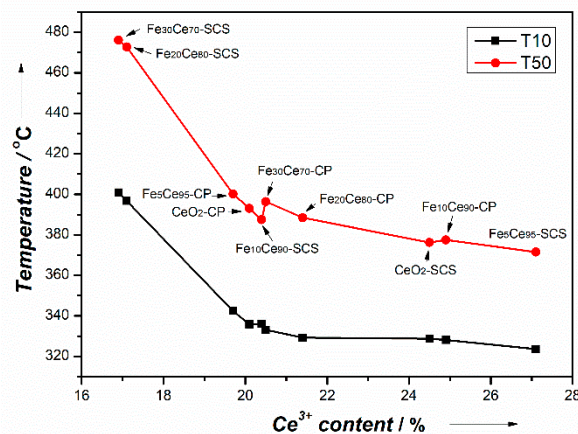


Figure 9. Relation between Ce³⁺ percentage and T10, T50.

H₂-TPR results showed that 10%-CP and 5%-SCS led to the highest reducibility and, therefore, the highest activity, which is in agreement with XPS and Raman results. For SCS catalysts with iron doping, more bulk oxygen becomes releasable and can be more easily transferred to surface oxygen and oxidize soot. This makes the diffusion of bulk oxygen very important for SCS catalysts. However, for CP catalysts, the bulk oxygen reduction peaks were almost unchanged, implying that the Fe doping does not influence the bulk oxygen reduction.

Herein, the different activities of the as-produced catalysts were due to their different morphologies, lattice distortion and changed surface properties based on various iron doping. When the Fe doping ratio was lower than 5%, SCS catalysts showed better activity towards soot oxidation regardless of their low BET surface area. This is due to their porous structure, high surface oxygen vacancy concentration and better reducibility of surface oxygen. However, when the Fe doping ratio exceeds 10%, CP catalyst performed better, which can be attributed to their relative higher surface oxygen vacancies.

3. Materials and Methods

3.1. Preparation of the Catalysts

Fe_xCe_{100-x}-CP ($x = 5; 10; 20; \text{ and } 30$ in percent of molar ratio) catalysts were synthesized by co-precipitation (CP). A stoichiometric solution of iron nitrate nonahydrate (Sigma-Aldrich, CAS:

7782-61-8, 99.95% trace metals basis) and cerium nitrate hexahydrate (Sigma-Aldrich, Saint Louis, MO, USA, CAS: 10294-41-4, 99.999% trace metals basis) were dissolved separately in deionized water, then mixed together with vigorous agitation. The aqueous ammonia (Sigma-Aldrich, CAS:1336-21-6, 28–30% NH₃ basis) was then gradually dropped into the above-mentioned solution under stirring conditions until pH reached 8.5, after which the solution was aged in air for one day at room temperature with constant stirring. The resultant precipitates were separated by vacuum filtration with three washes with deionized water. The obtained precipitates were dried at 100 °C for 12 h and then calcined at 500 °C for 5 h in static air. For comparison, pure cerium oxide-CeO₂ was prepared using a similar procedure.

Fe_xCe_{100-x}-SCS ($x = 5; 10; 20$; and 30 in percent of molar ratio) catalysts were obtained by solution combustion synthesis (SCS). An aqueous solution of iron nitrate nonahydrate (Sigma-Aldrich, CAS: 7782-61-8, 99.95% trace metals basis), cerium nitrate hexahydrate (Sigma-Aldrich, CAS: 10294-41-4, 99.999% trace metals basis) and glycine (Sigma-Aldrich, CAS: 56-40-6) in a stoichiometric ratio was prepared under vigorous stirring at 90 °C to form the gel. Then, the gel was combusted on a heating plate. The combustion procedure is very fast, producing fine powders. The resultant sample was then calcined at 500 °C for 5 h. CeO₂-SCS catalyst was developed using a similar procedure. The Fe content was examined using EDX (Energy-dispersive X-ray spectroscopy), and the results are shown in Table 4.

Table 4. Fe contents for the 5 and 10% catalysts as determined from EDX.

| Atomic % | 5% Fe-CP | 5% Fe-SCS | 10% Fe-CP | 10% Fe-SCS |
|----------|----------|-----------|-----------|------------|
| Fe | 5.5 | 5.9 | 9.3 | 11.7 |

3.2. Characterization of the Catalysts

X-ray powder diffraction (XRD) analysis was performed on X-ray powder diffractometer (German Bruker D4 (40 kV, 30 mA), Billerica, MA, USA, with position-sensitive detector and CuK α radiation). The XRD patterns were recorded in steps of 0.01° with a scanning rate of 5°/min from 5° to 85°. The diffraction peaks were indexed according to the Powder Data File database (PDF 2004, International Centre of Diffraction Data, Pennsylvania).

The surface area was measured by means of N₂ adsorption-desorption isotherms using Beishide 3H-2000PS2 static volumetric method analyzer (Beijing, China). The surface areas of catalysts were evaluated by Brunauer-Emmett-Teller (BET) method.

The morphologies, microstructures and elemental composition of the obtained catalysts were characterized by a Field-emission scanning electron microscope (FE-SEM, Zeiss MERLIN with Gemini-II column).

X-ray photoelectron spectroscopy (XPS) measurements were carried out on ESCALab220i-XL electron spectrometer (VG Scientific Ltd., Loughborough, UK) with 300 W AlK α X-ray source equipment to investigate the oxidation states of cerium and iron, and availability of oxygen on catalyst surface. The calibration of binding energies was conducted by using C1s peaks at 284.8 eV. Spectra-fits were performed with Gaussian-Lorentzian functions by using CasaXPS software.

The Raman spectra of the catalysts were measured on a Renishaw InVia micro laser Raman spectrometer (Renishawplc, Wotton-under-Edge, UK) with a 4mW Ar+ laser source ($\lambda_{\text{exc}} = 532 \text{ nm}$) with a cooled CCD detector at room temperature to differentiate chemical structures. The acquisition time was 60s and the scanning range was 100–800 cm⁻¹.

Temperature-programmed reduction with H₂ (H₂-TPR) experiments was carried out to study the reducibility of the catalyst by using a Micromeritics Autochem II 2920 analyzer (Norcross, GA, USA) with a thermal conductivity detector (TCD). 30 mg catalyst was first pre-treated at 150 °C for 1 h under 40 mL/min N₂ flow to remove water and other contaminants and then cooled down to room temperature. TPR analysis was conducted by heating up the sample to 1000 °C at 10 °C /min in a flow of 40 mL/min 10% H₂/Ar.

3.3. Catalytic Activity Tests

Thermogravimetric analysis (TGA) of catalytic soot oxidation was conducted on a TA Instrument Q500 apparatus to investigate catalytic activity. Printex-U carbon black (Chicago, IL, USA), with particulate size of 25 nm and $100 \text{ m}^2\text{g}^{-1}$ surface area, was used as a model of soot. Tight contact conditions of mixed sample were obtained by grinding soot and catalyst with a weight ratio of 1:9 in an agate mortar for 10 min. For each TGA test, a weighted amount of 10 mg sample was pre-treated at 150°C under 60 mL/min Nitrogen for 30 min to remove water and other contaminants. Then, the sample was heated up to 800°C under 40 mL/min air with a heating rate of $10^\circ\text{C}/\text{min}$. The thermogravimetric curves were obtained by continuously recording the mass change, along with increased temperature. Each TGA test was repeated three times to ensure the repeatability of the results. The activity of catalyst was evaluated by T10 and T50. T10 is commonly used as the ignition temperature, which is the temperature at 10% conversion of soot [1,20,22,52]. T50 is the combustion temperature, identified as the temperature when 50% of soot is oxidized [1,2,22,52].

4. Conclusions

Distinct morphologies of iron-doped ceria catalyst with different Fe doping ratios were prepared by co-precipitation and solution combustion methods, for catalyzing soot oxidation. It was confirmed by XRD that iron was incorporated in the cerium oxide lattice, although a limited amount of iron oxides may exist in the catalyst. The main conclusions of this study are:

1. Irrespective of the fabrication method, the most important parameter that dictates the reaction activity (e.g., T50) is the Ce^{3+} content, which is closely related to the content of oxygen vacancies.
2. The activity increases notably when Ce^{3+} content increases up to 20% (T50 from 476°C at 17% Ce^{3+} down to 393°C at 20% Ce^{3+}). Above 20% Ce^{3+} content, the activity increases moderately (T50 of 372°C at 27% Ce^{3+}).
3. For both fabrication methods, there is an optimum Fe content that gives the highest activity. For SCS catalyst, the optimum Fe content is 5%, and for CP catalyst, it is 10%.
4. The pore size is mostly about 3–5 nm (both CP and SCS), which is much smaller than the 25 nm soot particles used here. This is why, although the BET surface area is greater for CP than SCS, it has only moderate effect on the activity.
5. The catalyst preparation method has a profound impact on the catalyst morphology. The CP catalyst shows a dense spherical morphology, whereas the SCS catalyst has a spongy structure with large openings, around 250 nm, which can be large enough for soot particles to penetrate in and contact with the catalyst. Therefore, it can be anticipated that more soot particle can deposit on the SCS catalyst.

Supplementary Materials: The following materials are available online at <http://www.mdpi.com/2073-4344/9/10/815/s1>, Figure S1: Deconvoluted TPR results for CP catalysts, Figure S2: Deconvoluted TPR results for SCS catalysts, Table S1: H_2 consumption of CP catalysts, Table S2. H_2 consumption of CP catalysts.

Author Contributions: B.L. prepared the samples, conducted the experiments, analyzed the data and wrote this paper. J.Z.W. and E.C. led and oversaw the University of Waterloo part of this work—specifically the catalyst fabrication and experiments. A.R. provided initial consultants.

Funding: This research was funded by Natural Sciences and Engineering Research Council of Canada (NSERC) and BioFuelNet Canada.

Acknowledgments: The authors would thank the Key Laboratory of Coal Science and Technology at Taiyuan University of Technology for helping characterize the catalysts using Raman and H_2 -TPR spectroscopy.

Conflicts of Interest: The authors declare no conflict of interest.

References

1. Andana, T.; Piumetti, M.; Bensaid, S.; Russo, N.; Fino, D.; Pirone, R. Nanostructured ceria-praseodymia catalysts for diesel soot combustion. *Appl. Catal. B Environ.* **2016**, *197*, 125–137.

2. Venkataswamy, P.; Jampaiah, D.; Rao, K.N.; Reddy, B.M. Nanostructured $\text{Ce}_{0.7}\text{Mn}_{0.3}\text{O}_{2-\delta}$ and $\text{Ce}_{0.7}\text{Fe}_{0.3}\text{O}_{2-\delta}$ solid solutions for diesel soot oxidation. *Appl. Catal. A Gen.* **2014**, *488*, 1–10.
3. Soler, L.; Casanovas, A.; Escudero, C.; Pérez-Dieste, V.; Aneggi, E.; Trovarelli, A.; Llorca, J. Ambient Pressure Photoemission Spectroscopy Reveals the Mechanism of Carbon Soot Oxidation in Ceria-Based Catalysts. *ChemCatChem* **2016**, *8*, 2748–2751.
4. Bueno-López, A. Diesel soot combustion ceria catalysts. *Appl. Catal. B Environ.* **2014**, *146*, 1–11.
5. Fino, D.; Bensaïd, S.; Piumetti, M.; Russo, N. A review on the catalytic combustion of soot in Diesel particulate filters for automotive applications: From powder catalysts to structured reactors. *Appl. Catal. A Gen.* **2016**, *509*, 75–96.
6. Neyertz, C.A.; Banus, E.D.; Miró, E.E.; Querini, C.A. Potassium-promoted $\text{Ce}_{0.65}\text{Zr}_{0.35}\text{O}_2$ monolithic catalysts for diesel soot combustion. *Chem. Eng. J.* **2014**, *248*, 394–405. [[CrossRef](#)]
7. Oi-Uchisawa, J.; Obuchi, A.; Wang, S.; Nanba, T.; Ohi, A. Catalytic performance of Pt/ MO_x loaded over SiC-DPF for soot oxidation. *Appl. Catal. B Environ.* **2003**, *43*, 117–129.
8. Neeft, J.P.A.; Makkee, M.; Moulijn, J.A. Diesel particulate emission control. *Fuel Process. Technol.* **1996**, *47*, 1–69. [[CrossRef](#)]
9. Burch, R. Knowledge and Know-How in Emission Control for Mobile Applications. *Catal. Rev.* **2004**, *46*, 271–334. [[CrossRef](#)]
10. Russell, A.; Epling, W.S. Diesel Oxidation Catalysts. *Catal. Rev.* **2011**, *53*, 337–423.
11. Eastwood, P. *Critical Topics in Exhaust Gas Aftertreatment*; Publisher: Washington, DC, USA, 2000.
12. Bueno-López, A.; Krishna, K.; van der Linden, B.; Mul, G.; Moulijn, J.A.; Makkee, M. On the mechanism of model diesel soot- O_2 reaction catalysed by Pt-containing La^{3+} -doped CeO_2 : A TAP study with isotopic O_2 . *Catal. Today* **2007**, *121*, 237–245. [[CrossRef](#)]
13. Nagai, Y.; Hirabayashi, T.; Dohmae, K.; Takagi, N.; Minami, T.; Shinjoh, H.; Matsumoto, S. Sintering inhibition mechanism of platinum supported on ceria-based oxide and Pt-oxide-support interaction. *J. Catal.* **2006**, *242*, 103–109. [[CrossRef](#)]
14. Wei, Y.; Zhao, Z.; Liu, J.; Xu, C.; Jiang, G.; Duan, A. Design and Synthesis of 3D Ordered Macroporous CeO_2 -Supported Pt@ $\text{CeO}_{2-\delta}$ Core-Shell Nanoparticle Materials for Enhanced Catalytic Activity of Soot Oxidation. *Small* **2013**, *9*, 3957–3963. [[CrossRef](#)] [[PubMed](#)]
15. Liu, S.; Wu, X.; Weng, D.; Ran, R. Ceria-based catalysts for soot oxidation: A review. *J. Rare Earths* **2015**, *33*, 567–590. [[CrossRef](#)]
16. López-Haro, M.; Pérez-Omil, J.; Hernández-Garrido, J.; Trasobares, S.; Hungría, A.; Cies, J.; Midgley, P.; Bayle-Guillemaud, P.; Martínez-Arias, A.; Bernal, S. Advanced Electron Microscopy Investigation of Ceria-Zirconia-Based Catalysts. *ChemCatChem* **2011**, *3*, 1015–1027. [[CrossRef](#)]
17. Kopelent, R.; van Bokhoven, J.A.; Szlachetko, J.; Edebeli, J.; Paun, C.; Nachtegaal, M.; Safonova, O.V. Catalytically active and spectator Ce^{3+} in ceria-supported metal catalysts. *Angew. Chem. Int. Ed.* **2015**, *54*, 8728–8731. [[CrossRef](#)]
18. Shelef, M.; McCabe, R. Twenty-five years after introduction of automotive catalysts: What next? *Catal. Today* **2000**, *62*, 35–50. [[CrossRef](#)]
19. Heck, R.M.; Farrauto, R.J. Automobile exhaust catalysts. *Appl. Catal. A Gen.* **2001**, *221*, 443–457. [[CrossRef](#)]
20. Zhang, Z.; Han, D.; Wei, S.; Zhang, Y. Determination of active site densities and mechanisms for soot combustion with O_2 on Fe-doped CeO_2 mixed oxides. *J. Catal.* **2010**, *276*, 16–23. [[CrossRef](#)]
21. Setiabudi, A.; Chen, J.; Moulijn, J.A.; Mul, G.; Makkee, M. CeO_2 catalysed soot oxidation: The role of active oxygen to accelerate the oxidation conversion. *Appl. Catal. B Environ.* **2004**, *51*, 9–19. [[CrossRef](#)]
22. Miceli, P.; Bensaïd, S.; Russo, N.; Fino, D. Effect of the morphological and surface properties of CeO_2 -based catalysts on the soot oxidation activity. *Chem. Eng. J.* **2015**, *278*, 190–198. [[CrossRef](#)]
23. Liu, J.; Zhao, Z.; Wang, J.; Xu, C.; Duan, A.; Jiang, G.; Yang, Q. The highly active catalysts of nanometric CeO_2 -supported cobalt oxides for soot combustion. *Appl. Catal. B Environ.* **2008**, *84*, 185–195. [[CrossRef](#)]
24. Muroyama, H.; Hano, S.; Matsui, T.; Eguchi, K. Catalytic soot combustion over CeO_2 -based oxides. *Catal. Today* **2010**, *153*, 133–135. [[CrossRef](#)]
25. Li, X.; Wei, S.; Zhang, Z.; Zhang, Y.; Wang, Z.; Su, Q.; Gao, X. Quantification of the active site density and turnover frequency for soot combustion with O_2 on Cr doped CeO_2 . *Catal. Today* **2011**, *175*, 112–116. [[CrossRef](#)]

26. Li, H.; Li, K.; Wang, H.; Zhu, X.; Wei, Y.; Yan, D.; Cheng, X.; Zhai, K. Soot combustion over $Ce_{1-x}Fe_xO_{2-\delta}$ and CeO_2/Fe_2O_3 catalysts: Roles of solid solution and interfacial interactions in the mixed oxides. *Appl. Surf. Sci.* **2016**, *390*, 513–525. [[CrossRef](#)]
27. Thomas, J.M.; Raja, R. Mono-, Bi- and Multifunctional Single-Sites: Exploring the Interface Between Heterogeneous and Homogeneous Catalysis. *Top. Catal.* **2010**, *53*, 848–858. [[CrossRef](#)]
28. An, K.; Somorjai, G.A. ChemInform Abstract: Nanocatalysis I: Synthesis of Metal and Bimetallic Nanoparticles and Porous Oxides and Their Catalytic Reaction Studies. *Catal. Lett.* **2015**, *145*, 233–248. [[CrossRef](#)]
29. Agarwal, S.; Lefferts, L.; Mojet, B.L. Ceria nanocatalysts: Shape dependent reactivity and formation of OH. *ChemCatChem* **2013**, *5*, 479–489. [[CrossRef](#)]
30. Yuan, Q.; Duan, H.-H.; Li, L.-L.; Sun, L.-D.; Zhang, Y.-W.; Yan, C.-H. Controlled synthesis and assembly of ceria-based nanomaterials. *J. Colloid Interface Sci.* **2009**, *335*, 151–167. [[CrossRef](#)]
31. Wei, Y.; Zhao, Z.; Yu, X.; Jin, B.; Liu, J.; Xu, C.; Duan, A.; Jiang, G.; Ma, S. One-pot synthesis of core-shell $Au@CeO_2$ -[small delta] nanoparticles supported on three-dimensionally ordered macroporous ZrO_2 with enhanced catalytic activity and stability for soot combustion. *Catal. Sci. Technol.* **2013**, *3*, 2958–2970. [[CrossRef](#)]
32. Yamazaki, K.; Kayama, T.; Dong, F.; Shinjoh, H. A mechanistic study on soot oxidation over CeO_2 -Ag catalyst with ‘rice-ball’ morphology. *J. Catal.* **2011**, *282*, 289–298. [[CrossRef](#)]
33. Wei, Y.; Liu, J.; Zhao, Z.; Duan, A.; Jiang, G. The catalysts of three-dimensionally ordered macroporous $Ce_{1-x}Zr_xO_2$ -supported gold nanoparticles for soot combustion: The metal-support interaction. *J. Catal.* **2012**, *287*, 13–29. [[CrossRef](#)]
34. Zhang, G.; Zhao, Z.; Liu, J.; Jiang, G.; Duan, A.; Zheng, J.; Chen, S.; Zhou, R. Three dimensionally ordered macroporous $Ce_{1-x}Zr_xO_2$ solid solutions for diesel soot combustion. *Chem. Commun.* **2010**, *46*, 457–459. [[CrossRef](#)] [[PubMed](#)]
35. Bensaid, S.; Russo, N.; Fino, D. CeO_2 catalysts with fibrous morphology for soot oxidation: The importance of the soot-catalyst contact conditions. *Catal. Today* **2013**, *216*, 57–63. [[CrossRef](#)]
36. Piumetti, M.; Bensaid, S.; Russo, N.; Fino, D. Nanostructured ceria-based catalysts for soot combustion: Investigations on the surface sensitivity. *Appl. Catal. B Environ.* **2015**, *165*, 742–751. [[CrossRef](#)]
37. Palmisano, P.; Russo, N.; Fino, P.; Fino, D.; Badini, C. High catalytic activity of SCS-synthesized ceria towards diesel soot combustion. *Appl. Catal. B Environ.* **2006**, *69*, 85–92. [[CrossRef](#)]
38. Wang, H.; Luo, S.; Zhang, M.; Liu, W.; Wu, X.; Liu, S. Roles of oxygen vacancy and O_x^- in oxidation reactions over CeO_2 and Ag/CeO_2 nanorod model catalysts. *J. Catal.* **2018**, *368*, 365–378. [[CrossRef](#)]
39. Katta, L.; Sudarsanam, P.; Thrimurthulu, G.; Reddy, B.M. Doped nanosized ceria solid solutions for low temperature soot oxidation: Zirconium versus lanthanum promoters. *Appl. Catal. B Environ.* **2010**, *101*, 101–108. [[CrossRef](#)]
40. Lin, X.; Li, S.; He, H.; Wu, Z.; Wu, J.; Chen, L.; Ye, D.; Fu, M. Evolution of oxygen vacancies in MnO_x - CeO_2 mixed oxides for soot oxidation. *Appl. Catal. B Environ.* **2018**, *223*, 91–102. [[CrossRef](#)]
41. Lee, J.H.; Lee, S.H.; Choung, J.W.; Kim, C.H.; Lee, K.-Y. Ag-incorporated macroporous CeO_2 catalysts for soot oxidation: Effects of Ag amount on the generation of active oxygen species. *Appl. Catal. B Environ.* **2019**, *246*, 356–366. [[CrossRef](#)]
42. Liu, S.; Wu, X.; Tang, J.; Cui, P.; Jiang, X.; Chang, C.; Liu, W.; Gao, Y.; Li, M.; Weng, D. An exploration of soot oxidation over CeO_2 - ZrO_2 nanocubes: Do more surface oxygen vacancies benefit the reaction? *Catal. Today* **2017**, *281*, 454–459. [[CrossRef](#)]
43. Tang, Y.; Qiao, H.; Wang, H.; Tao, P. Nanoparticulate $Mn_{0.3}Ce_{0.7}O_2$: A novel electrocatalyst with improved power performance for metal/air batteries. *J. Mater. Chem. A* **2013**, *1*, 12512. [[CrossRef](#)]
44. Sahoo, T.R.; Armandi, M.; Arletti, R.; Piumetti, M.; Bensaid, S.; Manzoli, M.; Panda, S.R.; Bonelli, B. Pure and Fe-doped CeO_2 nanoparticles obtained by microwave assisted combustion synthesis: Physico-chemical properties ruling their catalytic activity towards CO oxidation and soot combustion. *Appl. Catal. B Environ.* **2017**, *211*, 31–45. [[CrossRef](#)]
45. Perez-Alonso, F.J.; Granados, M.L.; Ojeda, M.; Terreros, P.; Rojas, S.; Herranz, T.; Fierro, J.L.G.; Gracia, M.; Gancedo, J.R. Chemical Structures of Coprecipitated Fe–Ce Mixed Oxides. *Chem. Mater.* **2005**, *17*, 2329–2339. [[CrossRef](#)]
46. Aneggi, E.; De Leitenburg, C.; Dolcetti, G.; Trovarelli, A. Promotional effect of rare earths and transition metals in the combustion of diesel soot over CeO_2 and CeO_2 - ZrO_2 . *Catal. Today* **2006**, *114*, 40–47. [[CrossRef](#)]

47. Barbato, P.S.; Colussi, S.; Di Benedetto, A.; Landi, G.; Lisi, L.; Llorca, J.; Trovarelli, A. CO preferential oxidation under H₂-rich streams on copper oxide supported on Fe promoted CeO₂. *Appl. Catal. A Gen.* **2015**, *506*, 268–277. [[CrossRef](#)]
48. Radutoiu, N.; Teodorescu, C. Satellites in Ce 3d X-Ray Photoelectron Spectroscopy of Ceria. *Dig. J. Nanomater. Biostruct. (DJNB)* **2013**, *8*, 1535–1549.
49. Sudarsanam, P.; Mallesham, B.; Durgasri, D.N.; Reddy, B.M. Physicochemical characterization and catalytic CO oxidation performance of nanocrystalline Ce–Fe mixed oxides. *RSC Adv.* **2014**, *4*, 11322–11330. [[CrossRef](#)]
50. Jampaiah, D.; Tur, K.M.; Ippolito, S.J.; Sabri, Y.M.; Tardio, J.; Bhargava, S.K.; Reddy, B.M. Structural characterization and catalytic evaluation of transition and rare earth metal doped ceria-based solid solutions for elemental mercury oxidation. *RSC Adv.* **2013**, *3*, 12963–12974. [[CrossRef](#)]
51. Wang, W.; Zhu, Q.; Qin, F.; Dai, Q.; Wang, X. Fe doped CeO₂ nanosheets as Fenton-like heterogeneous catalysts for degradation of salicylic acid. *Chem. Eng. J.* **2018**, *333*, 226–239. [[CrossRef](#)]
52. Piumetti, M.; Bensaid, S.; Russo, N.; Fino, D. Investigations into nanostructured ceria–zirconia catalysts for soot combustion. *Appl. Catal. B Environ.* **2016**, *180*, 271–282. [[CrossRef](#)]



© 2019 by the authors. Licensee MDPI, Basel, Switzerland. This article is an open access article distributed under the terms and conditions of the Creative Commons Attribution (CC BY) license (<http://creativecommons.org/licenses/by/4.0/>).